energies

Article

Optimal Microgrid Protection Coordination for Directional Overcurrent Relays Through Mixed-Integer Linear Optimization

León F. Serna-Montoya [1,*], Sergio D. Saldarriaga-Zuluaga [2], Jesús M. López-Lezama [1,*] and Nicolás Muñoz-Galeano [1]

[1] Research Group on Efficient Energy Management (GIMEL), Department of Electrical Engineering, Universidad de Antioquia (UdeA), Medellín 050010, Colombia; nicolas.munoz@udea.edu.co
[2] Departamento de Eléctrica, Facultad de Ingeniería, Institución Universitaria Pascual Bravo, Calle 73 No. 73A-226, Medellín 050036, Colombia; s.saldarriagazu@pascualbravo.edu.co
* Correspondence: leon.serna@udea.edu.co (L.F.S.-M.); jmaria.lopez@udea.edu.co (J.M.L.-L.)

Abstract: Microgrids (MGs) are revolutionizing modern power systems by enabling decentralized energy production, renewable energy integration, and enhanced grid resilience. However, the increasing complexity of MGs, particularly with the integration of Distributed Energy Resources (DERs), poses significant challenges for traditional protection schemes. This study addresses the coordination of Directional Overcurrent Relays (DOCRs) in MGs through a Mixed-Integer Linear Programming (MILP) model. The main contribution is a MILP model that optimizes relay settings, including Time Multiplier Settings (TMS) and standard characteristic curves, to minimize tripping times, while ensuring selectivity. Another key contribution of this work is the integration of both IEC and IEEE standard curves, which enhances coordination performance compared to using a single standard. The model was tested on the IEC benchmark microgrid, and the results demonstrated significant improvements in fault-clearing times across various operational modes. By leveraging advanced optimization techniques and diverse characteristic curves, this study contributes to the development of resilient and efficient protection systems for modern microgrids, ensuring reliable operation under varying fault conditions and DER penetration.

Keywords: distributed generation; microgrid; power system protection; overcurrent relay coordination; directional overcurrent relay; mixed-integer linear programming; optimization

check for updates

Academic Editor: Tek Tjing Lie

Received: 7 March 2025
Revised: 8 April 2025
Accepted: 13 April 2025
Published: 16 April 2025

Citation: Serna-Montoya, L.F.; Saldarriaga-Zuluaga, S.D.; López-Lezama, J.M.; Muñoz-Galeano, N. Optimal Microgrid Protection Coordination for Directional Overcurrent Relays Through Mixed-Integer Linear Optimization. *Energies* **2025**, *18*, 2035. https://doi.org/10.3390/en18082035

Copyright: © 2025 by the authors. Licensee MDPI, Basel, Switzerland. This article is an open access article distributed under the terms and conditions of the Creative Commons Attribution (CC BY) license (https://creativecommons.org/licenses/by/4.0/).

1. Introduction

Microgrids (MGs) are set to revolutionize the power grid, but their increasing complexity requires robust and adaptable protection systems. The need for renewable energy integration, distributed generation, and enhanced grid resiliency drives the rapid integration of MGs into modern power systems. Microgrids offer the ability to operate in both grid-connected and islanded modes, providing flexibility and reliability to the power system [1,2]. However, the increasing penetration of renewable energy sources in MGs presents unique challenges for traditional protection schemes, potentially leading to cascading failures and system instability. Furthermore, the penetration of Distributed Energy Resources (DERs) such as solar photovoltaic (PV), wind turbines, and energy storage systems has transformed fault characteristics, making traditional protection schemes insufficient [3,4].

Directional Overcurrent Relays (DOCRs) are the most widely used protection devices in microgrid systems, due to their simplicity and cost-effectiveness [5,6]. However, coordinating DOCRs in MGs with high penetration of DERs presents unique challenges, including

bidirectional fault currents, variable fault levels, and the need for adaptive settings. Existing protection coordination approaches often rely on standard IEEE or IEC characteristic curves [7–9]. Recent research highlights the importance of integrating non-standard curves and employing advanced optimization techniques to overcome these limitations [10,11].

Despite these advancements, challenges persist. The dependency on communication infrastructure for centralized protection schemes can introduce vulnerabilities, especially in scenarios involving communication delays or failures [12,13]. To address this issue, recent studies have proposed communication-free protection schemes [12], aiming to enhance reliability by eliminating the need for real-time communication between relays. Additionally, fault detection techniques such as those based on differential admittance angles and data-driven methods have shown potential for improving accuracy and speed, but their practical implementation remains an open issue [14].

Adaptive protection schemes for MGs enhance resilience by dynamically adjusting protection settings and coordination strategies in response to changing operating conditions and fault scenarios. Research by Jahanbani et al. [15] focused on tailoring protection for high renewable energy penetration, while Alasali et al. [16] and Sati et al. [17] explored hybrid deep learning models to improve fault detection and classification. Peter et al. [18] investigated innovative hybrid model designs and feature selection for enhanced performance, and Reiz et al. [19] addressed cybersecurity concerns by developing robust models resistant to malicious attacks.

Communication-free protection schemes enhance microgrid resilience by eliminating the need for centralized communication, thereby mitigating the risks associated with communication delays, failures, and cyberattacks. Heidary et al. [20] explored the performance of communication-free schemes in detecting and isolating faults, while Asghari et al. [21] proposed novel schemes utilizing artificial intelligence for autonomous decision-making at each protection device. Ghanem et al. [22] investigated the vulnerabilities of existing schemes to communication disruptions, guiding the development of more robust communication-free alternatives. Vazquez et al. [23] focused on tailoring communication-free protection to specific microgrid applications, such as residential or industrial settings. Finally, Yan et al. [24] explored the use of advanced technologies, such as specialized sensors and embedded processors, to facilitate local decision-making and coordination within communication-free protection systems. Supporting this perspective, Wang et al. [25] presented a comprehensive study on real-time reconfiguration of protective devices under varying load and renewable generation conditions. Their approach leverages dynamic system data to adjust protection settings on-the-fly, thereby enhancing microgrid resilience and selectivity.

The IEC benchmark has been used to establish a general framework for comparing results, and emerging trends using IEC benchmarks have shown the complexity of fault detection and classification, exposing the limitations of traditional techniques. For instance, ref. [26] proposed a wavelet-based ensembled intelligent technique, validated using the IEC microgrid benchmark, which demonstrated superior fault detection and classification performance compared to conventional methods. Similarly, ref. [27] introduced a novel approach leveraging the Teager–Kaiser Energy Operator and micro-Phasor Measurement Units (μPMUs) to extract energy signatures for real-time event detection, validated through simulations of an integrated microgrid model. Addressing uncertainties in fault detection, ref. [28] developed a deep-learning-based protection scheme that adapts to dynamic conditions, enhancing system resilience. Furthermore, ref. [29] advanced sub-cycle fault detection using advanced signal processing techniques, validated with standardized benchmarks, to meet stringent time requirements. Collectively, these studies underscored the critical role of standardized benchmarks, such as the IEC microgrid model, in driving inno-

vation and addressing diverse challenges in microgrid protection and fault management. This article presents a well-detailed benchmark MG that can be used as a test framework for research purposes.

The hardware-in-the-loop (HIL) and digital twin methodologies are vital for validating the effectiveness and robustness of protection schemes in realistic microgrid environments. Alasali et al. [30] utilized HIL testing to rigorously evaluate the performance of protection systems under diverse operating conditions, including varying loads, renewable energy generation, and fault scenarios. Dewangan et al. [31] leveraged digital twin simulations to comprehensively assess the impact of various fault scenarios, including transient events and cyberattacks, on protection system behavior. Bui et al. [32] integrated HIL testing with advanced data analytics to optimize protection settings and improve overall system performance. Khan et al. [33] employed digital twin technology as a virtual testbed for developing and testing novel protection algorithms before their deployment in real-world microgrids, reducing risks and accelerating the development process. Tripathy et al. [34] combined HIL testing with machine learning techniques to enhance the accuracy and adaptability of protection systems in dynamic MG environments, enabling them to effectively respond to changing operating conditions and unforeseen events.

The coordination of overcurrent devices addresses a critical gap in previous research by integrating both IEC and IEEE characteristic curves for enhanced protection coordination performance. Biswal et al. [35] investigated the impact of integrating diverse characteristic curves on coordination performance and system reliability, demonstrating the potential for improved selectivity and reduced misoperation rates. Cisneros-Saldana et al. [36] developed an optimization framework that leverages both IEC and IEEE curves to minimize coordination times, while ensuring selectivity constraints. Singh et al. [37] analyzed the influence of different combinations of IEC and IEEE curves on the performance of protection systems in various microgrid configurations. Desai et al. [38] proposed a novel approach for selecting the optimal combination of IEC and IEEE curves based on real-time operating conditions and fault characteristics.

Many scientific reports have explored the application of advanced metaheuristic algorithms for optimal relay coordination of microgrids. These algorithms, particularly well-suited for tackling non-linear and large-scale optimization problems, offer promising solutions for complex microgrid protection schemes. In [39], the authors showed the effectiveness of the Genetic Algorithm (GA), Harmony Search (HS), Imparialist Competitive Algorithm (ICA), and Firefly Algorithm (FA) for achieving optimal relay coordination, ensuring proper selectivity and minimizing tripping times. Kumar et al. [40] explored the potential of the JAYA algorithm for optimal relay coordination, focusing on its efficiency and robustness in finding optimal solutions. Abdi et al. [5] applied the Harmony Search algorithm to optimize relay settings, demonstrating its effectiveness in handling complex microgrid configurations with multiple distributed energy resources. Sadeghi et al. [12] utilized a novel metaheuristic algorithm inspired by natural phenomena for optimal relay coordination, emphasizing its ability to handle uncertainties and achieve robust protection performance. Merabet et al. [41] compared the performance of various metaheuristic algorithms for relay coordination, providing valuable insights into their strengths and weaknesses in the context of microgrid protection. Metaheuristic algorithms such as NSGA-II, JAYA, and the Water Cycle Algorithm (WCA) have demonstrated the capability to minimize relay operating times, while ensuring selectivity constraints [40]. These methods have shown promising results in addressing the nonlinear and discrete nature of the DOCR coordination problem. Moreover, studies such as [35] have emphasized the role of hybrid optimization techniques that combine metaheuristics with machine learning to improve fault detection and relay coordination.

In contrast, exact models offer distinct advantages when solving coordination problems in microgrids using overcurrent protection. Their deterministic nature ensures consistent results, and exact solvers guarantee global optimality, providing precise solutions to well-defined problems. Linear models are computationally efficient for small- to medium-sized systems and benefit from mature, well-supported solvers that facilitate rapid convergence. Additionally, their simplicity and structured formulation make them easier to interpret and analyze, ensuring strict compliance with constraints. These models often rely on linear approximations of inherently non-linear relationships in microgrid systems. In general, linear models have long been widely reported in the scientific literature. However, in many studies, the Time Multiplier Setting (TMS) is considered as the only decision variable, while other parameters are treated as constants [42], which limits the search space. Some studies focus solely on using a single characteristic curve, typically the IEC Standard Inverse (SI) curve [43]. More recent research has expanded this approach to include multiple curve selections [44]. The most advanced models incorporate both IEC and IEEE curves within a mixed-integer linear programming (MILP) framework. However, these models introduce undesirable factors that affect the objective function, and they have not yet been validated in MG environments [45].

Recent studies have faced significant limitations, due to their reliance on non-linear models, which are typically solved using metaheuristic techniques. Scientific evidence indicates that metaheuristic algorithms are capable of finding local optima; however, their performance is highly dependent on parameter selection and fine-tuning. In contrast, a Mixed-Integer Linear Programming (MILP) model guarantees a global optimum and follows a deterministic process, ensuring consistency in the obtained solutions. This paper builds on this existing body of knowledge by addressing several key gaps in the following ways.

- A MILP-based model for protection coordination is developed. The primary advantage of exact models, such as MILP, is their ability to guarantee a global optimum, whereas non-linear models only ensure local optima and usually require metaheuristic techniques for their resolution. Metaheuristic methods incorporate stochastic components to explore different regions of the solution space, allowing them to escape local optima and identify improved solutions. However, this inherent randomness makes metaheuristics non-deterministic, while MILP remains a structured and predictable optimization approach.
- The performance of protection coordination schemes that integrate both IEEE and IEC standards is evaluated, comparing them to those that rely solely on the IEEE standard. Most exact models reported in the technical literature use only one IEC curve, and while some approaches allow the evaluation of multiple IEC curves, no studies have tested the combined use of IEC and IEEE standards. This gap exists despite growing research trends advocating for the integration of both standards, to enhance relay coordination performance.

Although exact models for parameter coordination exist, their application to microgrids has not been explored. Additionally, the integration of IEEE curves without impacting the objective function remains unaddressed. This study applies an advanced optimization framework with diverse characteristic curves to assess protection system performance in microgrids, ensuring reliable operation under varying fault conditions and DER penetration levels.

This article is structured as follows: Section 1 addresses recent contributions from the scientific community, focusing on studies related to protection coordination in MGs employing overcurrent protection. Section 2 describes the ANSI 51 inverse time protection, including the types of curves defined by both IEC and IEEE standards, centralized and de-

centralized protection schemes, as well as adaptive and directional protection. Additionally, it provides a comprehensive description of the IEC benchmark microgrid. The MILP model is also presented in detail in this section, explaining all parameters, decision variables, and the objective functions. Section 3 presents the operational modes considered. The results highlight the shorter tripping times and offer a detailed description of the outcomes for each operational mode. Finally, Section 4 summarizes the key findings of the study, supported by the results described in the preceding sections.

2. Methodology

Protection of power systems is a critical aspect of ensuring operational reliability, safety, and stability. Among the various protection mechanisms, overcurrent protection is a key part of the fault detection and isolation process, thereby preventing equipment damage and minimizing system downtime. This section examines the principles and methods of inverse-time overcurrent protection, with particular emphasis on ANSI 51 standard [46], which is widely used in power distribution and industrial systems. By exploring operating characteristics, coordination strategies, and advanced features such as adaptive and directional protection, this section provides a comprehensive understanding of how modern protection schemes are designed to meet the challenges of increasingly complex power systems. It also examines the integration of centralized and distributed control approaches, highlighting their respective advantages and limitations in achieving robust and efficient fault management. To further improve protection coordination, a MILP model is introduced that aims to minimize relay operating times, while ensuring selectivity, through the optimal selection of TMS and standard curve types. This model, formulated as an assignment problem, incorporates key parameters such as PSM and Coordination Time Intervals (CTIs), and provides a systematic framework for optimizing relay settings in various operating scenarios. Through this discussion, this section aims to detail the relevant background and the proposed MILP model.

2.1. Inverse-Time Protection ANSI 51

Protection function 51 refers to a time-overcurrent protection and is a mechanism in power system protection schemes. Its primary purpose is to detect and isolate faults by measuring current levels that exceed predefined thresholds for a specified time delay. This section provides a detailed description of the operating principles, characteristics, and applications of ANSI 51 protection. Time-overcurrent protection is widely utilized in distribution networks and industrial systems as an effective means of detecting overcurrent conditions caused by faults, such as short circuits or overloads. Unlike instantaneous overcurrent protection (ANSI 50), which operates without intentional delay, the 51 function incorporates a time-delay characteristic, enhancing coordination with other protection devices.

The 51 protection function operates based on a predefined time–current characteristic curve. When the current flowing through the system exceeds the pickup value (I_pickup), the protection relay initiates a timing process. The relay trips the circuit breaker if the fault persists for a duration exceeding the specified time delay. The time delay is inversely proportional to the magnitude of the fault current, following one of several standardized curves. The performance of 51 protection is defined by its pickup current setting, TMS, and the selected time–current curve. These parameters allow fine-tuning of the relay's response to ensure proper coordination with upstream and downstream devices in the protection hierarchy.

Time-overcurrent protection offers several advantages, making it a widely used scheme in power system protection. Its simplicity and cost-effectiveness are among its primary strengths, as the function requires minimal computational resources and can be easily

implemented in both electromechanical and digital relays. Additionally, it provides reliable fault detection and isolation in radial systems, where the power flow is unidirectional and straightforward coordination is feasible. However, 51 protection has limitations that restrict its applicability in more complex network topologies. For instance, in meshed networks, its selectivity is often inadequate without the integration of directional elements or adaptive coordination strategies.

The 51 protection function offers flexibility and reliability for fault detection and coordination. Advances in digital relays and communication technologies have further enhanced its capabilities, enabling adaptive and coordinated protection strategies in complex systems like MGs.

2.1.1. IEC Standard Curves

The time–current curves for inverse-time overcurrent relays are defined by the IEC 60255 standard [47], which specifies various time-delay characteristics to adapt the relay's behavior to the requirements of each application. These curves, such as the standard inverse, very inverse, and extremely inverse, are designed to ensure proper coordination with other protection devices within the electrical system. The trip time can be adjusted using the TMS parameter, which allows for fine-tuning of the protection response.

Table 1 presents the standard coefficients A, B, and C used for the IEC-standardized time–current curves; it includes the most widely used coefficients associated with IEC-defined curves, which are crucial for determining the operating time of overcurrent relays. These coefficients A, B, and C are applied in the characteristic equations of the time–current curves, ensuring flexibility and precision in configuring protection systems. For instance, the "IEC Standard Inverse" curve is suitable for general applications, while curves like "IEC Extremely Inverse" or "IEC Ultra-Inverse" are tailored for specific scenarios, such as transformer protection or highly inductive loads. Each curve's response depends on the interplay between these coefficients and the TMS.

Table 1. Standard coefficients for calculating the operating time of IEC standard curves.

Curve Type	C	B	A
IEC Extremely Inverse (EI)	0	2	80
IEC Long Time Inverse (LTI)	0	1	120
IEC Short Time Inverse (STI)	0	0.04	0.05
IEC Standard Inverse (SI)	0	0.02	0.14
IEC Ultra-Inverse (UI)	0	2.5	315.2
IEC Very Inverse (VI)	0	1	13.5

2.1.2. IEEE Standard Curves

The time–current curves for inverse-time overcurrent relays are also well-defined under standard IEEE C37.112 [48], which specifies various time-delay characteristics tailored to the requirements of electrical systems. These curves, such as the moderately inverse, very inverse, and extremely inverse, are designed to ensure a reliable coordination. The trip time of the relay is calculated using characteristic equations defined by the IEEE, with the time delay being adjustable via the TMS parameter, providing flexibility in achieving optimal protection and coordination.

Table 2 lists the standard coefficients A, B, and C used for the IEEE-standardized time–current curves. These coefficients are integral to the characteristic equations that define the trip time of the relay, ensuring adaptability to various fault conditions and coordination requirements. For example, the moderately inverse curve is commonly used for feeders, while the extremely inverse curve is more suitable for protecting transformers.

Each curve's operating time is influenced by the fault current magnitude and the TMS parameter, enabling precise relay coordination across different protection zones. These terms were adapted from the IEEE C37.112 standard, unifying the nomenclature between both standards (IEC and IEEE).

Table 2. Standard coefficients for calculating the operating time of IEEE standard curves.

Curve Type	C	B	A
IEEE Extremely Inverse (EI)	0.1217	2	28.2
IEEE Long Time Extremely Inverse (LTEI)	0.25	2	64.07
IEEE Long Time Inverse (LTI)	0.185	0.05	0.086
IEEE Long Time Very Inverse (LTVI)	0.712	2	28.55
IEEE Moderately Inverse (MI)	0.114	0.02	0.0515
IEEE Short Time Extremely Inverse (STEI)	0.005	2	1.281
IEEE Short Time Inverse (STI)	0.11858	0.02	0.16758
IEEE Very Inverse (VI)	0.491	2	19.61

2.1.3. Adaptive and Directional Features

Adaptive and directional overcurrent protection are advanced methodologies designed to enhance the reliability and flexibility of protection systems in modern power networks. Adaptive overcurrent protection dynamically adjusts settings according to real-time system conditions, including load variations, network topology changes, and fault characteristics. This approach ensures optimal coordination between protection devices, reducing the risk of misoperations and improving the system's resilience against disturbances. Directional overcurrent protection, on the other hand, incorporates directional elements to determine the flow of fault current relative to the relay location. This feature is critical in systems with bidirectional power flows, such as MGs or renewable energy-integrated networks, where traditional overcurrent protection may fail to distinguish between forward and reverse faults. By combining adaptivity and directional capabilities, protection systems can address the challenges posed by complex and evolving grid configurations, ensuring fast, selective, and reliable fault clearance.

2.1.4. Centralized and Decentralized Control in Protection System

Centralized control relies on a single control entity, often located at a control center, to collect data from all system components, analyze it, and send commands to protection devices. This approach offers advantages such as global coordination, optimal decision-making, and efficient fault management. However, centralized systems are highly dependent on communication infrastructure and are vulnerable to single points of failure, which may affect reliability in real-time operations.

In contrast, decentralized control distributes the decision-making process among multiple local controllers, typically embedded in the protection devices themselves. Each controller operates autonomously, relying on locally available information to execute protection actions. Decentralized systems are inherently more resilient to communication failures and offer faster response times, as they eliminate the need for centralized data processing. However, achieving effective coordination between devices in decentralized systems can be challenging, especially in interconnected or dynamic networks.

Both control approaches have their merits and limitations, and their application depends on the specific requirements of the power system. Hybrid control schemes that integrate the strengths of centralized and decentralized approaches are increasingly being explored to enhance the robustness and flexibility of protection systems in complex grid environments.

2.2. Microgrid Benchmark Framework

This section provides a comprehensive overview of the IEC Microgrid benchmark, initially introduced in [49] and later expanded in [50]. Benchmarks have been used in the research and development of power systems, particularly in microgrid studies, by offering a structured testing environment. The IEC benchmark microgrid is widely recognized for enabling direct comparisons between various protection and control strategies under identical operating conditions. Its design integrates practical constraints and operational scenarios, bridging the gap between theoretical research and real-world applications.

Benchmark Description

The parameters presented in Table 3 characterize the utility connection of the benchmark IEC microgrid. The utility is modeled with a rated short-circuit power of 1000 MVA, providing the necessary fault level for stability and protection coordination studies. The system operates at a frequency of 60 Hz, with a rated and base voltage of 120 kV. These parameters establish the utility's contribution to the microgrid's performance, including its impact on fault current levels, voltage regulation, and overall system dynamics. The high short-circuit power ensures a strong grid connection, making it suitable for analyzing various operating conditions and disturbances.

Table 3. Utility parameters.

Parameter	Value	Unit
Rated short-circuit power	1000	MVA
Frequency (f)	60	Hz
Rated voltage	120	kV
Base voltage (V_{base})	120	kV

Table 4 presents the parameters of the distributed generators (DGs) used in the benchmark microgrid. DG1 and DG2 are modeled as synchronous generators with a rated power of 9 MVA each, operating at 2.4 kV and 60 Hz. Their dynamic behavior is characterized by an inertia constant of 1.07 s, a friction factor of 0.1 pu, and various reactance and time constants that define their electrical and transient performance. DG3 represents an inverter-based wind farm consisting of three turbines, each rated at 2 MVA with a power factor of 0.9, resulting in a total rated capacity of 6 MVA. It operates at a voltage level of 575 kV and has an inertia constant of 0.62 s. The electrical parameters for DG3, including reactances and time constants, are defined to reflect its inverter-based operation. Both types of DGs include parameters for the resistance, reactances along the d- and q-axes, leakage reactance, and time constants associated with open-circuit transient and sub-transient states. These parameters provide a detailed representation of the generators' behavior, enabling the study of dynamic responses, fault scenarios, and system stability within the MG.

Table 5 provides the parameters for DG4, a wind farm based on a doubly fed induction generator (DFIG). The wind farm has a total rated capacity of 9 MVA, composed of six turbines, each rated at 1.5 MVA, operating at 575 V and 60 Hz. Its dynamic characteristics are defined by an inertia constant of 0.685 s and a friction factor of 0.01 pu, which influence its response to system disturbances.

Electrical parameters of DG4 include a stator resistance (R_s) of 0.023 pu, rotor resistance (R'_r) of 0.016 pu, and their respective leakage inductances, L_s and L'_r, of 0.18 pu and 0.16 pu. The magnetizing inductance (L_m) is specified as 2.9 pu, reflecting the generator's capability to sustain magnetic flux linkage. These parameters model the performance and interaction of the DFIG-based wind farm within a microgrid, particularly under dynamic and transient conditions.

Table 4. Parameters of DGs.

Parameter	DG1, DG2 Synchronous Generators	DG3 Inverter-Based Wind Farm
Rated MVA	9	6 $pf = 0.9$ (three turbines, 2 MVA each)
Frequency (f)	60 Hz	60 Hz
Rated voltage	2.4 kV	575 kV
Inertia constant (H)	1.07 s	0.62 s
Friction factor (F)	0.1 pu	0.1 pu
Resistance (R_s)	0.0036 pu	0.006 pu
d-axis reactance (X_d)	1.56 pu	1.305 pu
d-axis transient reactance (X'_d)	0.296 pu	0.296 pu
d-axis sub-transient reactance (X''_d)	0.177 pu	0.252 pu
q-axis reactance (X_q)	1.06 pu	0.474 pu
q-axis sub-transient reactance (X''_q)	0.177 pu	0.243 pu
Leakage reactance (X_l)	0.052 pu	0.18 pu
Open-circuit transient time constant (T'_{d0})	3.7 s	4.49 s
Open-circuit sub-transient time constant (T''_{d0})	0.05 s	0.0681 s
q-axis subtransient time (T_q0'')	0.05 s	0.0513 s

Table 5. DG4: DFIG-based Wind Farm Parameters.

Parameter	Value
Rated MVA	9 (six turbines, 1.5 MVA each)
Frequency (f)	60 Hz
Rated voltage	575 V
Inertia constant (H)	0.685 s
Friction factor (F)	0.01 pu
Stator resistance (R_s)	0.023 pu
Stator leakage inductance (L_s)	0.18 pu
Rotor resistance (R'_r)	0.016 pu
Rotor leakage inductance (L'_r)	0.16 pu
Magnetizing inductance (L_m)	2.9 pu

Table 6 outlines the parameters of the transformers (TRs) utilized in the benchmark microgrid. The transformers serve different connections within the system, each tailored to the specific requirements of the connected components. TR1, rated at 15 MVA, operates with a voltage ratio of 120/25 kV, reflecting its role in interfacing the utility grid with the distribution network. TR2 and TR3, each rated at 12 MVA, step up the voltage from 2.4 kV to 25 kV for synchronous generators DG1 and DG2. TR4, with a 10 MVA capacity, steps up the voltage from 575 V to 25 kV, accommodating wind farms DG3 and DG4. All transformers operate at 60 Hz and share common electrical characteristics, including a winding resistance (R_1) of 0.00375 pu, a leakage reactance (X_1) of 0.01 pu, and magnetizing parameters (R_m and X_m) of 500 pu each.

Table 7 presents the parameters of the distribution lines (DL). Each line spans a length of 30 km and operates at a base voltage of 25 kV. The lines are modeled using both resistance and inductance parameters for zero-sequence (R_0 and L_0) and positive-sequence (R_1 and L_1) components, allowing for detailed representation of electrical characteristics under balanced and unbalanced conditions.

Table 6. Transformer (TR) parameters.

Transformer	TR1	TR2, TR3	TR4
Rated MVA	15	12	10
Frequency (f)	60 Hz	60 Hz	60 Hz
Rated voltage	120/25 kV	2.4/25 kV	575/25 kV
Base voltage (V_{base})	120 kV	25 kV	25 kV
Winding resistance (R_1)	0.00375 pu	0.00375 pu	0.00375 pu
Leakage reactance (X_1)	0.01 pu	0.01 pu	0.01 pu
Magnetizing resistance (R_m)	500 pu	500 pu	500 pu
Magnetizing reactance (X_m)	500 pu	500 pu	500 pu

The resistance values are specified as 0.1153 Ω/km for zero-sequence and 0.413 Ω/km for positive-sequence. The corresponding inductance values are 1.05×10^{-3} H/km for zero-sequence and 3.32×10^{-3} H/km for positive-sequence. Additionally, the lines' capacitive effects are characterized by a zero-sequence capacitance (C_0) of 11.33×10^{-9} F/km and a positive-sequence capacitance (C_1) of 5.01×10^{-9} F/km.

Table 7. Distribution lines (DLs) parameters.

Parameter	**Value**	**Unit**
Line length	30	km (per line)
Base voltage (V_{base})	25	kV
Line resistance (R_0)	0.1153	Ω/km
Line resistance (R_1)	0.413	Ω/km
Inductance (L_0)	1.05×10^{-3}	H/km
Inductance (L_1)	3.32×10^{-3}	H/km
Capacitance (C_0)	11.33×10^{-9}	F/km
Capacitance (C_1)	5.01×10^{-9}	F/km

Figure 1 illustrates the structure of an IEC benchmark microgrid, designed to represent a typical distribution system with multiple DERs. The system consists of a primary utility connection at the Point of Common Coupling (PCC), labeled as B-1, with the main circuit breaker (CB_MAIN) connected to Transformer TR-1. The microgrid operates in a radial configuration, branching into three feeders, each equipped with protection devices, including relays (R-1 to R-10), circuit breakers (CB_LOOP1, CB_LOOP2), and interconnection lines (DL-1 to DL-5). Each feeder supplies energy to distributed generators (DG-1 to DG-4) through step-down transformers (TR-2 to TR-5), providing realistic representation of both grid-connected and islanded operational modes. The microgrid's loads (L-1 to L-6) and buses (B-2 to B-6) enable the simulation of fault scenarios, load variations, and switching events, supporting advanced research in protection coordination, fault detection, and optimization. The total loading (sum of L1 to L6) considered is 22 MW, 10 MVAR.

Table 8 specifies that the column I_{pickup} represents the pickup current, which is determined by the load for each relay. The locations of the relays within the IEC microgrid are illustrated in Figure 1. The current transformer ratio (CTR) for all relays is 400, except for relay R7, which has a CTR of 1200.

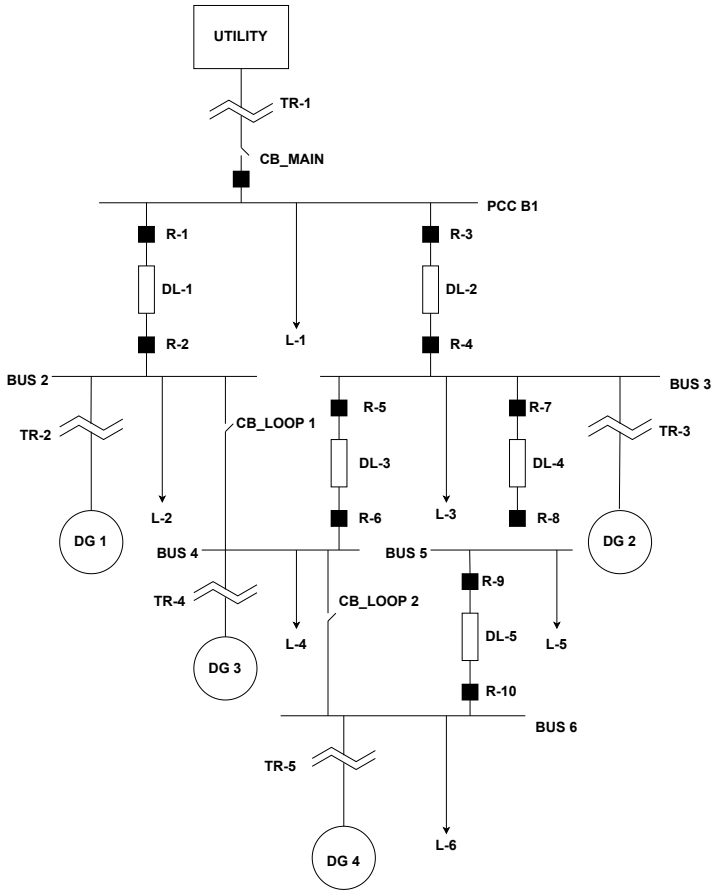


Figure 1. IEC benchmark microgrid.

Table 8. *CTR* and i_{pickup} with each relay.

Relay	I_{pickup}
R1, R2, R3, R4, R5, R6, R8, R9, R10, R12	0.50
R7	1.00
R11, R14	0.65
R13	0.88
R15	0.55

2.3. Mixed-Integer Linear Model

This section provides a detailed description of the implemented optimization model. The model definition begins with the definition of the sets, followed by the parameters and variables involved. The formulation incorporates the objective function and constraints, capturing the essential elements of the problem under study. The objective is to minimize the sum of the operating times for each DOCR by optimizing the relay settings, specifically the TMS and the standard characteristic curve (SCC) type. This optimization is carried out while ensuring compliance with selectivity constraints. In this study, a CTI constant of 0.3 s was used for consistency and to facilitate comparisons with existing scientific literature.

2.3.1. Sets

The optimization model employs a set-based framework to structure its key components. The set R represents the collection of relays in the system. The set F captures the faults perceived by each relay across different operating modes, ensuring that the model accommodates the system's dynamic behavior under various fault scenarios. Additionally,

the set C encompasses the standard inverse-time overcurrent curves, providing a range of predefined options to tailor the relay settings.

- R: Represents the relays in the system.
- F: Set of faults detected by each relay in each operating mode.
- C: Set of standard curves.

2.3.2. Parameters

Equation (1) defines the plug setting multiplier (PSM_{if}) for each relay $i \in R$ and each fault $f \in F$. It relates the short-circuit current (ICC_{if}) observed for the relay to the pick-up current ($Ipickup_i$) of each relay. This Equation (1) ensures that PSM_{if} is calculated for all relays and faults.

$$PSM_{if} = \frac{ICC_{if}}{Ipickup_i} \quad \forall \quad i \in R, \quad f \in F \tag{1}$$

Equation (2) defines β_{fic}. The parameter β_{fic} is a key element that facilitates the linearization of the optimization model, transforming the nonlinear problem into an assignment problem. The constants A_c, B_c, and C_c correspond to each type of SCC, with their specific values listed in Table 1 for IEC curves and Table 2 for IEEE curves. Notice that subindex $c \in C$ depicts curves in the set C. The value of PSM_{if} derived from Equation (1) incorporates the short-circuit current and pick-up current.

$$\beta_{fic} = \frac{A_c}{PSM_{if}^{B_c} - 1} \quad \forall \quad i \in R, \quad f \in F, \quad c \in C \tag{2}$$

The parameter BU, defined in Equation (3), establishes the relationship between primary relays and their corresponding backup relays. It is important to note that $ij \neq ji$, as the selectivity principle of the system, dictates that the backup relationship is not interchangeable. This parameter plays a crucial role in ensuring proper coordination within the protection scheme, where each relay's backup is explicitly identified.

$$BU_{ij} = \begin{cases} 1, & \text{relay } j \text{ is the backup of relay } i \quad \forall \quad i, j \in R \\ 0, & \text{relay } j \text{ is NOT the backup of relay } i \quad \forall \quad i, j \in R \end{cases} \tag{3}$$

2.3.3. Model

The following is the proposed mixed-integer linear model, accompanied by a description of the constraints. The general objective is to minimize the tripping time of the DOCRs in the MG for each fault. The decision variables include the set of offline configurations for each relay. A centralized controller identifies the OM and communicates the settings to the relays to achieve the minimum operating time across the defined scenarios, taking into account an adaptive function. The decision variables are the TMS (TMS_{ic}) and SCC $c \in C$. Note that the model is formulated as an assignment problem for optimization. Therefore, TMS_{ic} is sized for all relays times of the available curves, but its selection depends on non-zero values. The auxiliary variable x_{ic} allows the model to select a single curve for each relay, which allows the upper and lower boundary conditions to be set.

$$\min \sum_{i \in R} \sum_{f \in F} t_{if} \tag{4}$$

Subject to

$$t_{if} = \sum_{c \in C} (\beta_{fic} TMS_{ic} + x_{ic} C_c) \quad \forall \quad i \in R, \quad f \in F, \quad \beta_{fic} \geq 0 \tag{5}$$

$$\sum_{c \in C} (\beta_{fjc} TMS_{jc} + x_{jc} C_c) - t_{if} \geq CTI$$

$$\forall \quad i, j \in R : i \neq j, \quad f \in F, \quad \beta_{fic} \geq 0, \quad \beta_{fjc} \geq 0, \quad BU_{ij} = 1 \tag{6}$$

$$\sum_{c \in C} x_{ic} = 1 \quad \forall \quad i \in R \tag{7}$$

$$TMS_{ic} \leq TMS_{ub} x_{ic} \quad \forall \quad i \in R, \quad c \in C \tag{8}$$

$$TMS_{ic} \geq TMS_{lb} x_{ic} \quad \forall \quad i \in R, \quad c \in C \tag{9}$$

$$t_{if} \geq 0 \quad \forall \quad i \in R, \quad f \in F \tag{10}$$

$$TMS_{ic} \geq 0 \quad \forall \quad i \in R, \quad c \in C \tag{11}$$

$$x_{ic} \in \{0, 1\} \quad \forall \quad i \in R, \quad c \in C \tag{12}$$

Equation (4) defines the objective function of the optimization model, which aims to minimize the sum of relay tripping times. The variable t_{if} represents the tripping time (in seconds) of each relay $i \in R$ under fault $f \in F$. The constraints of the optimization model are described below.

Constraint (5): This constraint calculates the operating time t_{if} as the product of the parameter β_{fic} and the decision variable TMS_{ic}, plus the curve constant C_c times x_{ic}. The parameter β_{fic} embeds the PSM, as described in Equation (1). Only the selected curve contributes to the calculation, since $TMS_{ic} = 0$ for unselected curves.

Constraint (6): This selectivity constraint ensures a CTI between the operating time of the primary relay i and its backup relay j, both $\in R$. The parameters β_{fic} and β_{fjc} are only considered when greater than zero, as negative values indicate that they are not faults, because the sensed current is lower than I_{pickup} (refer to Equation (2) for further details). As mentioned above, i and j must be different because they are a backup arrangement. BU_{ij} is 1 if relay j is the backup of relay i, otherwise 0.

Constraint (7): The decision variable x_{ic} ensures that exactly one curve $c \in C$ is selected for each relay $i \in R$. This variable influences the bounds for TMS_{ic}, enabling proper curve assignment.

Constraints (8) and (9): These represent the upper and lower bounds, respectively, for the time multiplier setting (TMS). When $x_{ic} = 0$, this forces $TMS_{ic} = 0$, ensuring that only one curve $c \in C$ is selected. The model assumes those boundaries $TMS_{ub} = 1$ and $TMS_{lb} = 0.001$.

The domain of the decision variables is defined by Equations (10)–(12). These equations constrain the variables as follows: First, $t_{if} \geq 0 \, \forall i \in R, f \in F$, is a continuous variable representing the operating time (in seconds) of relay i under fault f. This variable is minimized in the objective function to ensure optimal relay operation. Second, $TMS_{ic} \geq 0 \, \forall i \in R, c \in C$, is a continuous variable representing the Time Multiplier Setting (TMS) for relay i when associated with the characteristic curve c. This variable determines the relay's tripping time based on the assigned curve and its parameters. Finally, $x_{ic} \in \{0, 1\} \, \forall i \in R, c \in C$ is a binary decision variable that indicates whether the characteristic curve c is assigned to relay i. Specifically, $x_{ic} = 1$ if curve c is selected for relay i, and $x_{ic} = 0$ otherwise. This variable ensures that each relay is assigned exactly one characteristic curve, enforcing the constraint $\sum_{c \in C} x_{ic} = 1$. Together, these variables and their domains form the foundation for formulation of the optimization problem.

The primary contribution of this study is the linearization that enables the selection of different types of standard curves within the protection coordination model, improving

upon the formulation presented in [45]. The model follows a classic assignment structure, where all curve coefficients (A, B, and C) are embedded in the parameter β_{fic}, working in harmony with the decision variables TMS_{ic} and x_{ic}. Specifically, the binary variable x_{ic} enforces the bounds on TMS_{ic}, while the constraint (7) ensures that only one curve is selected per relay. Consequently, TMS_{ic} determines the optimal curve that minimizes the relay operating time, given that t_{if} is linearly related to the objective function. When analyzing the optimal solution, numerous zero values appear in TMS_{ic}, corresponding to non-selected curves, whereas nonzero values indicate the selection of the most effective curve for improving the objective function.

The Coordination Time Interval (CTI) was set to 0.3 based on previous studies, although this parameter can typically range between 0.2 and 0.5. The boundary conditions were defined as 0.0001 and 1 for TMS_{lb} and TMS_{ub}, respectively, providing sufficiently flexible limits to allow the model to select an optimal TMS_{ic}. Regarding model limitations, the main constraint was the treatment of PSM_{if} as a parameter rather than a variable. Recent studies have formulated PSM as a variable, leading to nonlinear models that require heuristic solution techniques. This approach, however, does not guarantee global optimality and introduces non-deterministic behavior, due to the inherent nature of nonlinear models. In contrast, the MILP formulation proposed in this study ensures global optimality, achieving improved relay operating times compared to some previous works that treated PSM_{if} as a variable.

3. Results

This section presents the results obtained, using the methods described in the previous section. Figure 2 illustrates the systematic methodology for designing and implementing a robust protection scheme for MGs. The process began with the acquisition of MG data, which included DG parameters, transformer performance, distribution lines, MG topology, and component parameters, as detailed in Section 2.2. These data were then modeled using an electrical power analysis software, specifically DigSilent PowerFactory 2022 SP2, which facilitated the simulation of short circuits. Three-phase solidly grounded faults at 50% of each line were simulated using the IEC 60909 standard [51]. Subsequently, the short circuits observed by each relay were recorded, serving as input for the optimization model.

The optimization model incorporated MG topology data, including main and backup relay information, CT ratios, and pick-up currents. This model was developed using Pyomo 3.11, which is a Python-based modeling language for mathematical programming; it also considers performance criteria such as selectivity, sensitivity, and speed of operation (see Section 2.3 for details). The model was solved using the solver Highspy 1.26.4. Due to the nature of the problem, the solution contained numerous zeros, hindering direct interpretation. Therefore, Python 3.11.12 was employed to extract and identify the solution.

Recent research trends have significantly advanced the field of protection coordination in MGs. Studies have progressively reduced the tripping times of DOCRs by employing non-standard characteristics in reported analyses [52]. Conventionally, these studies rely on the set of curves defined by the IEEE or IEC standards (see Sections 2.1.1 and 2.1.2). However, the authors in [39] demonstrated reducing tripping times by integrating both standards in protection coordination studies. Consequently, this article evaluated two scenarios: (1) employing only the IEEE standard curves, and (2) incorporating both IEEE and IEC standards as part of the set C, the set of standard curves. The results obtained from this evaluation are presented in this section.

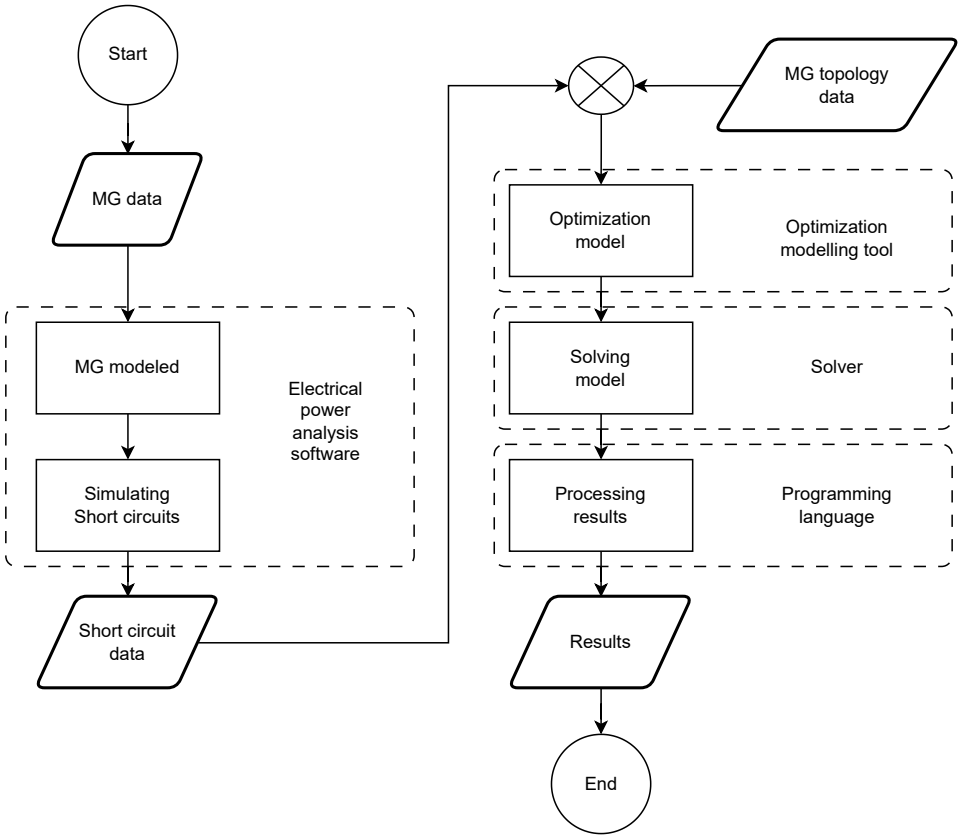


Figure 2. Systematic methodology for a protection scheme.

One of the key considerations for real-world implementation is the communication infrastructure required for optimal relay coordination. The proposed model assumes that relay settings can be adjusted dynamically, which would require a reliable and low-latency communication network to ensure real-time updates and coordination. Technologies such as IEC 61850 [53]-based communication protocols could facilitate the seamless integration of the optimization model into modern protection schemes.

Regarding integration with existing protection systems, the MILP model is designed to work with conventional directional overcurrent relays, meaning that its implementation would not require hardware modifications, but rather software-based updates to relay settings. Additionally, the model's ability to incorporate both IEC and IEEE standard curves enhances its applicability across various microgrid configurations.

To ensure practical feasibility and reliability, validation through hardware-in-the-loop (HIL) testing or real-time digital simulation (RTDS) would be an essential step before field deployment. These methods would allow assessing the model's performance under real operating conditions, verifying its effectiveness in handling different fault scenarios, and ensuring compliance with industry protection standards.

3.1. Operating Modes (OMs)

Table 9 outlines the operating modes considered in this study. Figure 1 illustrates the position of each DG unit and its associated bus. In Table 9, the text "enabled" indicates that the generation unit is supplying power to the grid, whereas the text "disabled" signifies that the unit is not contributing power to the network. In all scenarios analyzed in this article, the switches CB_LOOP1 and CB_LOOP2 were assumed to remain open. Additionally, grid connection was maintained in operating modes OM1, OM2, and OM3. Conversely, the

islanded mode was considered exclusively in operating mode OM4. These scenarios were used because most commercial relays have four sets of settings.

Table 9. Operating modes.

Operating Modes	Grid	GD1	GD2	GD3	GD4
OM1	enabled	disabled	disabled	disabled	disabled
OM2	enabled	enabled	enabled	enabled	enabled
OM3	enabled	enabled	enabled	disabled	disabled
OM4	disabled	enabled	enabled	enabled	enabled

3.2. Faults and Short-Circuit Currents

Table 10 presents the faults F1 to F5, detailing the lines where three-phase faults occurred at the midpoint of their length, identified as DL-1 to DL-5. The location of these lines within the IEC microgrid can be observed in Figure 1. The table header correlates the operating modes (OM1 to OM4) with the short-circuit currents, calculated using the IEC 60909 [51] method and expressed in kiloamperes. These calculations were performed through simulations in PowerFactory DIgSILENT. It is important to note that, as previously mentioned, the short-circuit levels demonstrated significant variations between different operating modes.

Table 10. Faults and short-circuit currents associated with each line.

Faults	Lines	OM1	OM2	OM3	OM4
F1	DL-5	3695	6296	4293	3941
F2	DL-4	5130	8725	6363	4158
F3	DL-2	8375	11,891	10,116	3558
F4	DL-1	5130	6989	6428	3188
F5	DL-3	3695	5904	4223	3590

3.3. Results for OM1

Table 11 presents the coordination parameters for the relays under OM1. The table compares two scenarios: one where both IEC and IEEE standard characteristic curves were considered, and another where only IEEE curves were included.

For each relay (R_i), the table specifies

- SCC_i: The standard characteristic curve assigned to the relay. Abbreviations such as “EI”, “VI”, “SI”, and “STEI” correspond to different IEC and IEEE curve types. Abbreviations are defined in Tables 1 and 2. A dash (-), on the other hand, indicates that there was no curve assigned for the relay in the current scenario.
- TMS_i: The TMS value optimized for the relay under the given scenario. TMS values reflect the operational configuration that minimized relay tripping times, while maintaining selectivity.

The left section of the table reports the results for the IEC and IEEE curves scenario, while the right section focuses on the IEEE-only scenario. Relays without an assigned curve are marked with dashes in both the SCC_i and TMS_i columns. For relays with assigned curves, the TMS_i values are provided, reflecting the optimal settings obtained through coordination studies.

Table 12 presents the tripping times (t_{if}) for relays under OM1 across two scenarios: one considering both IEC and IEEE standard curves, and the other considering only IEEE standard curves.

Table 11. Coordination parameters for OM1.

IEC and IEEE Curves			Only IEEE Curves		
Relay	SCC_i	TMS_i	**Relay**	SCC_i	TMS_i
R1	-	-	R1	-	-
R2	EI	0.0001	R2	IEEE-STEI	0.0001
R3	-	-	R3	-	-
R4	VI	0.3884	R4	IEEE-LTEI	0.2921
R5	-	-	R5	-	-
R6	LTI	0.1053	R6	IEEE-MI	0.6047
R7	SI	0.0000	R7	IEEE-LTVI	0.1730
R8	-	-	R8	-	-
R9	-	-	R9	-	-
R10	EI	0.0001	R10	IEEE-STEI	0.0001
R11	-	-	R11	-	-
R12	EI	0.0001	R12	IEEE-STEI	0.0001
R13	-	-	R13	-	-
R14	-	-	R14	-	-
R15	-	-	R15	-	-

For each fault $f \in F$, the table specifies

- Relay: The relay $i \in R$ that operated in response to the fault, considering the main and back up relays.
- t_{if} [s]: The operational time (in seconds) of the relay $i \in R$ for fault $f \in F$. This represents the time taken by the relay to trip after detecting the fault. Not only the main relays were considered, but the back up relays also contributed to calculating the total time.

The left section of the table corresponds to the scenario using both IEC and IEEE curves, while the right section shows the results for the IEEE-only scenario. For each fault, the relays involved and their respective tripping times are listed. At the bottom of the table, the total tripping times are provided, summing the operational times for all faults in each scenario. The results demonstrate a reduction in total tripping time when both IEC and IEEE curves were utilized, compared to using IEEE curves alone. Notice that when both sets (IEC and IEEE) were enabled, this OM1 preferred to use IEC only.

Table 12. Tripping times for OM1.

IEC and IEEE Curves			Only IEEE Curves		
Fault	**Relay**	t_{if} **[s]**	**Fault**	**Relay**	$t_i f$ **[s]**
F1	R2	0.0000	F1	R2	0.0050
F1	R4	0.3000	F1	R4	0.3050
F2	R4	0.2127	F2	R4	0.2785
F2	R6	0.5127	F2	R6	0.5785
F3	R6	0.3092	F3	R6	0.5155
F3	R7	0.6092	F3	R7	0.8155
F4	R7	0.7594	F4	R7	0.9979
F4	R12	0.0000	F4	R12	0.0050
F5	R6	0.7232	F5	R6	0.6325
F5	R10	0.0000	F5	R10	0.0050
Total time		3.43	Total time		4.14

3.4. Results for OM2

Table 13 presents the coordination parameters obtained from the optimization model for Operational Mode 2 (OM2). The results are shown for two scenarios: the first included

both IEC and IEEE standard characteristic curves, while the second considered only the IEEE curves. These scenarios allowed for an analysis of how the inclusion of additional curve standards impacted the coordination and tripping performance of DOCRs.

In the optimization model, each relay was assigned a standard characteristic curve (SCC_i), the model defines the set C, representing the available characteristic curves, where each relay i selects a specific curve $c \in C$ to determine its SCC_i, which determines its operational response to faults. The selection of SCC_i is a discrete decision made during the optimization process, based on its contribution to minimizing the total operating times of relays, while adhering to selectivity constraints. Additionally, the model computes the TMS_i, a continuous decision variable that directly influences the relay's tripping time. The optimization seeks to find the best combination of SCC_i and TMS_i for each relay, to ensure proper coordination and minimize the fault-clearing time.

The left-hand side of the table shows the results when both IEC and IEEE curves were available, providing a larger solution space and more flexibility for the optimization process. This flexibility generally resulted in lower t_{if} values and improved coordination. On the other hand, the right-hand side reflects the restricted scenario, where only IEEE curves were used.

Table 13. Coordination parameters for OM2.

IEC and IEEE Curves			Only IEEE Curves		
Relay	SCC_i	TMS_i	**Relay**	SCC_i	TMS_i
R1	EI	0.1975	R1	IEEE-EI	0.3423
R2	EI	0.0001	R2	IEEE-STEI	0.0001
R3	STI	0.0001	R3	IEEE-STEI	0.0001
R4	LTI	0.0556	R4	IEEE-LTI	0.0000
R5	EI	0.1904	R5	IEEE-EI	0.3300
R6	LTI	0.1068	R6	IEEE-LTVI	0.0000
R7	IEEE-LTI	0.4723	R7	IEEE-LTVI	0.1586
R8	EI	0.1480	R8	IEEE-EI	0.4932
R9	STI	0.0001	R9	IEEE-STEI	0.0001
R10	EI	0.0001	R10	IEEE-LTVI	−0.0000
R11	IEEE-LTVI	0.0429	R11	IEEE-VI	0.3596
R12	EI	0.0001	R12	IEEE-LTI	−0.0000
R13	IEEE-STI	0.0781	R13	IEEE-STI	0.0837
R14	IEEE-STI	0.0294	R14	IEEE-EI	0.0879
R15	IEEE-VI	0.0001	R15	IEEE-VI	0.0685

Table 14 provides the operating times (t_{if}) of DOCRs for OM2, comparing scenarios where both IEC and IEEE characteristic curves were included against scenarios with only IEEE curves. In the optimization model, t_{if} represents the tripping time of relay i under fault f, which was determined by the assigned characteristic curve (SCC_i) and its TMS_i. The objective of the optimization is to minimize the total operating time, while maintaining proper selectivity and coordination among the relays. The results in the left-hand column of the table show the optimized operating times when IEC and IEEE curves were available. This configuration achieved a total fault-clearing time of 8.54 s. In contrast, the right-hand column reflects the scenario restricted to IEEE curves only, where the total operating time increased to 10.55 s.

Table 14. Operating times for OM2.

IEC and IEEE Curves			Only IEEE Curves		
Fault	**Relay**	t_{if} **[s]**	**Fault**	**Relay**	t_{if} **[s]**
F1	R1	0.2362	F1	R1	0.2660
F1	R2	0.0000	F1	R2	0.0050
F1	R4	0.3000	F1	R4	0.3050
F1	R13	0.5362	F1	R13	0.5660
F2	R1	0.3001	F2	R1	0.3050
F2	R3	0.0001	F2	R3	0.0050
F2	R4	0.1890	F2	R4	0.2725
F2	R6	0.4890	F2	R6	0.5725
F2	R15	0.4911	F2	R15	0.5725
F3	R5	0.0883	F3	R5	0.1756
F3	R6	0.2831	F3	R6	0.5069
F3	R7	0.5831	F3	R7	0.8069
F3	R8	0.5831	F3	R8	0.8069
F3	R15	0.4912	F3	R15	0.6225
F4	R5	0.3000	F4	R5	0.3050
F4	R7	0.7722	F4	R7	1.0470
F4	R8	0.5026	F4	R8	0.7123
F4	R11	0.8026	F4	R11	1.0123
F4	R12	0.0000	F4	R12	0.0050
F5	R6	0.7972	F5	R6	0.6503
F5	R9	0.0001	F5	R9	0.0050
F5	R10	0.0000	F5	R10	0.0050
F5	R14	0.3001	F5	R14	0.3050
F5	R15	0.4913	F5	R15	0.7187
Total time		8.54	Total time		10.55

3.5. Results for OM3

Table 15 shows the parameter adjustments for DOCRs when employing IEC and IEEE characteristic curves versus exclusively using IEEE curves in OM3. The results reveal notable differences in the selection of SCC_i and their corresponding TMS_i. For the IEC and IEEE configuration, relays such as $R4$, $R5$, $R6$, $R7$, and $R8$ leveraged diverse curve types, including EI, IEEE-LTI, IEEE-VI, and VI, with TMS_i values tailored to minimize the overall operating times. In contrast, under the exclusive IEEE configuration, the SCC_i selections were predominantly oriented towards the IEEE-LTVI and IEEE-MI curves, which reflected the model's optimization goals under stricter curve availability.

Table 15. Coordination parameters for OM3.

IEC and IEEE Curves			Only IEEE Curves		
Relay	SCC_i	TMS_i	**Relay**	SCC_i	TMS_i
R1	-	-	R1	-	-
R2	EI	0.0001	R2	IEEE-STEI	0.0001
R3	-	-	R3	-	-
R4	VI	0.4548	R4	IEEE-LTVI	0.0000
R5	EI	0.0267	R5	IEEE-EI	0.0463
R6	VI	0.9695	R6	IEEE-MI	0.6115
R7	IEEE-LTI	0.4793	R7	IEEE-LTVI	0.1622
R8	EI	0.1495	R8	IEEE-EI	0.4948
R9	-	-	R9	-	-
R10	EI	0.0001	R10	IEEE-MI	0.0000

Table 15. *Cont.*

IEC and IEEE Curves			Only IEEE Curves		
Relay	SCC_i	TMS_i	**Relay**	SCC_i	TMS_i
R11	IEEE-EI	0.3291	R11	IEEE-LTVI	0.1431
R12	EI	0.0001	R12	IEEE-LTVI	0.0000
R13	-	-	R13	-	-
R14	-	-	R14	-	-
R15	IEEE-VI	0.0069	R15	IEEE-VI	0.0706

Table 16 presents the operating times for the relays in OM3, under two distinct scenarios: the combined use of IEC and IEEE characteristic curves, and the exclusive use of IEEE curves, similarly to the previous tables. The relays i, characteristic curves SCC_i, and operating times (t_{if}) for each fault $f \in F$ are shown. The results highlight that including IEC curves led to significantly reduced total operating times (t_{if}) compared to using only IEEE curves. This trend was particularly evident for faults such as $F3$ and $F4$, where the differences between configurations were most pronounced. These findings demonstrate how the diversity of characteristic curves contributes to more efficient coordination, minimizing response times and improving the selectivity of the protection system in complex microgrid scenarios.

Table 16. Operating times for OM3.

IEC and IEEE Curves			Only IEEE Curves		
Fault	**Relay**	$t_i f$ **[s]**	**Fault**	**Relay**	t_{if} **[s]**
F1	R2	0.0000	F1	R2	0.0050
F1	R4	0.3000	F1	R4	0.3050
F2	R4	0.1992	F2	R4	0.2750
F2	R6	0.4992	F2	R6	0.5750
F2	R15	0.4992	F2	R15	0.5750
F3	R5	0.1222	F3	R5	0.1963
F3	R6	0.2890	F3	R6	0.5090
F3	R7	0.5890	F3	R7	0.8090
F3	R8	0.5890	F3	R8	0.8090
F3	R15	0.5005	F3	R15	0.5880
F4	R5	0.3000	F4	R5	0.3050
F4	R7	0.7478	F4	R7	1.0032
F4	R8	0.5077	F4	R8	0.7141
F4	R11	0.8077	F4	R11	1.0141
F4	R12	0.0000	F4	R12	0.0050
F5	R6	0.7537	F5	R6	0.6394
F5	R10	0.0000	F5	R10	0.0050
F5	R15	0.5098	F5	R15	0.6827
Total time		7.21	Total time		9.01

3.6. Results for OM4

Table 17 shows the coordination parameters for OM4, detailing the selection of SCC_i and the corresponding TMS_i for each relay $i \in R$. The data are presented for two scenarios: the integration of IEC and IEEE characteristic curves, and the exclusive use of IEEE curves. Similarly to the previous tables, these data underscore the role of characteristic curves and TMS_i adjustments in optimizing the protection system's performance within OM4.

Table 17. Coordination parameters for OM4.

IEC and IEEE Curves			Only IEEE Curves		
Relay	SCC_i	TMS_i	**Relay**	SCC_i	TMS_i
R1	EI	0.1975	R1	IEEE-EI	0.3423
R2	STI	0.0001	R2	IEEE-STEI	0.0001
R3	STI	0.0001	R3	IEEE-STEI	0.0001
R4	EI	0.4893	R4	IEEE-EI	0.8479
R5	EI	0.4488	R5	IEEE-EI	0.7779
R6	IEEE-VI	0.0235	R6	IEEE-VI	0.0570
R7	-	-	R7	-	-
R8	EI	0.2065	R8	IEEE-EI	0.5214
R9	STI	0.0001	R9	IEEE-STEI	0.0001
R10	STI	0.0001	R10	IEEE-LTI	0.0000
R11	SI	0.1940	R11	IEEE-STI	0.1501
R12	STI	0.0001	R12	IEEE-STEI	0.0001
R13	VI	0.1462	R13	IEEE-LTI	0.3555
R14	STI	0.3300	R14	IEEE-LTI	0.0965
R15	IEEE-VI	0.0219	R15	IEEE-VI	0.0532

Table 18 presents the operating times for relays under OM4 across faults on its lines, comparing configurations with IEC and IEEE curves versus configurations with only IEEE curves. Each fault $f \in F$ is associated with its respective relay $i \in R$ and the time it took for the relay to operate t_{if}. For instance, fault $F1$ showed operation times ranging from 0.0000 s for $R2$ to 0.5362 s for $R13$ in the IEC and IEEE configuration, while in the IEEE-only configuration, $R13$ operated at 0.5660 s. Similar patterns are observed for the other faults, such as $F2$ and $F3$, where operating times varied depending on the selected curve settings.

The total operating time for all faults was 8.08 s for the IEC and IEEE curve configuration and 8.70 s for the IEEE-only configuration. This comparison highlights the influence of characteristic curve selection on the overall speed and performance of the protection system.

Table 18. Operating times for OM4.

IEC and IEEE Curves			Only IEEE Curves		
Fault	**Relay**	$t_i f$ **[s]**	**Fault**	**Relay**	$t_i f$ **[s]**
F1	R1	0.2362	F1	R1	0.2660
F1	R2	0.0000	F1	R2	0.0050
F1	R4	0.3000	F1	R4	0.3050
F1	R13	0.5362	F1	R13	0.5660
F2	R1	0.3001	F2	R1	0.3050
F2	R3	0.0001	F2	R3	0.0050
F2	R4	0.2171	F2	R4	0.2543
F2	R6	0.5171	F2	R6	0.5543
F2	R15	0.5171	F2	R15	0.5543
F3	R5	0.2081	F3	R5	0.2488
F3	R6	0.5137	F3	R6	0.5461
F3	R8	0.8137	F3	R8	0.8461
F3	R15	0.5331	F3	R15	0.5931
F4	R5	0.3000	F4	R5	0.3050
F4	R8	0.7013	F4	R8	0.7460
F4	R11	1.0013	F4	R11	1.0460
F4	R12	0.0000	F4	R12	0.0050
F5	R6	0.5370	F5	R6	0.6026
F5	R9	0.0001	F5	R9	0.0050
F5	R10	0.0000	F5	R10	0.0050

Table 18. *Cont.*

IEC and IEEE Curves			Only IEEE Curves		
Fault	**Relay**	$t_i f$ **[s]**	**Fault**	**Relay**	$t_i f$ **[s]**
F5	R14	0.3001	F5	R14	0.3050
F5	R15	0.5505	F5	R15	0.6355
Total time		8.08	Total time		8.70

3.7. Comparing Solver Performance

MILP is an exact optimization approach widely used to solve problems involving both continuous and integer variables; it builds on the foundation of linear programming, which provides exact solutions for convex problems, and extends it by incorporating integer constraints. The method ensures that the global optimum is found, provided the solver completes its process, making it a reliable tool for decision-making in various fields. However, the computational complexity of MILP is high, as it is classified as NP-hard, meaning that solving large-scale or highly complex problems can be time-consuming. Additionally, numerical precision issues in solvers may lead to minor deviations, but these do not detract from the exactness of the method within the specified tolerances.

In this study, the proposed MILP model was implemented using Pyomo 3.11, a Python-based optimization modeling language, and solved using the Highspy 1.26.4 solver. The computational times obtained are presented in Table 19. The problem formulation included a set of 15 relays (R), 5 fault scenarios (F), and a set of standard characteristic curves (C), where the IEC and IEEE scenario consisted of 13 curves. The parameter β_{fic}, which depends on the sets F, R, and C, had dimensions of 5 × 15 × 13, totaling 975 elements. Similarly, the parameter BU_{ij}, which defines the relationship between primary and backup relays, had a size of $|R|^2$. The optimization variables included relay operating times (t_{if}) with dimensions of 15 × 5 = 75, and time multiplier settings (TMS_{ic}) with a size of 15 × 13 = 195. Notably, this protection coordination problem was formulated as a classic assignment problem, meaning that only 15 values of TMS_{ic} were actively used (one per relay in R), while the remaining values were zero, indicating that the corresponding curve was not selected. Complementarily, the binary variable x_{ic} operated in harmony with TMS_{ic}, activating the appropriate bounds based on system constraints, and therefore also having a dimension of 195. In total, the MILP model consisted of 465 decision variables ($195 + 195 + 75$).

As highlighted in Table 19, the proposed approach exhibited promising computational efficiency, despite the NP-hard nature of MILP problems, where complexity typically increases exponentially with the number of variables. The solver successfully obtained solutions in all operational modes within a fraction of a second, with the highest recorded computation time being 0.4689 seconds. These results suggest that the proposed model is scalable to larger microgrid systems, while maintaining practical execution times. Although computational challenges may arise as system complexity increases, strategies such as problem decomposition, heuristic techniques, and parallel computing can further enhance scalability. Given the demonstrated performance, the MILP formulation provides a viable and efficient optimization framework for microgrid protection coordination, ensuring both feasibility and optimality within acceptable computational limits.

The NEOS Server (Network-Enabled Optimization System) [54] is an advanced, web-based platform that provides access to a wide range of state-of-the-art optimization solvers and computational resources. In this study, NEOS was used to solve the MILP model. Since MILP problems are exact in nature, all solvers are expected to converge to the same objective function value. However, the computational time required to reach the optimal

solution can vary significantly depending on the solver and its algorithmic approach. By employing multiple solvers available through NEOS, this section presents a comparison of their computational performance. This analysis provides insight into the efficiency of the solvers by evaluating the computational time spent.

Table 19. Computational time for MILP across different operating modes.

Operating Mode	Objective Function [s]	Computational Time [s]
OM1	3.43	0.2280
OM2	8.54	0.4689
OM3	7.21	0.3341
OM4	8.08	0.2114

Table 20 presents the computational performance of the various solvers when applied to the proposed MILP model, considering two scenarios: one incorporating both IEC and IEEE characteristic curves, and another restricted to IEEE curves only. The results highlight differences in solver efficiency, which were influenced by their algorithmic strategies and underlying heuristics, the values shown are given in seconds. Among the tested solvers, CBC and CPLEX demonstrated competitive performance, with CBC achieving relatively lower solution times in several cases. Bonmin showed longer computation times in the IEC and IEEE scenario, but performed efficiently in the IEEE-only scenario. FilMINT and Knitro achieved the lowest computational times in several operational modes, particularly for OM1 and OM2, suggesting their efficiency in handling mixed-integer formulations. MOSEK and MINLP-B&B exhibited significant variability in performance, with MOSEK showing longer computation times for OM4 in the IEC and IEEE case, while MINLP-B&B showed a drastic increase in OM2 for the IEEE-only scenario. These findings underscore the importance of solver selection when addressing complex MILP formulations, as different algorithms may exhibit varying degrees of efficiency depending on the problem structure. Only some solver versions were included in Table 20 whenever the specific version information is not available [54].

Table 20. Comparing solver performance.

Solver	IEC and IEEE Curves [s]				Only IEEE Curves [s]			
	OM1	OM2	OM3	OM4	OM1	OM2	OM3	OM4
Bonmin	19.4436	35.7948	29.9936	23.7276	5.6240	8.2846	8.8576	8.2851
CBC 2.10.10	7.2476	4.0430	2.8149	6.6674	14.1536	9.3852	8.1661	12.7109
CPLEX 22.1.1.0	9.3426	9.9889	8.3067	7.3701	9.8933	12.1769	7.0564	3.7548
FilMINT	2.5353	2.6633	4.0133	2.6262	4.3461	6.1379	2.5652	17.1957
Knitro 14.2.0	1.9598	2.4792	6.5178	4.9522	6.8008	4.1001	7.1931	2.6398
MINLP-B&B (20100607)	16.4559	17.5753	6.2411	2.8193	3.1074	19.1533	4.1572	3.3868
Minto	16.2404	15.7236	2.1112	2.0364	3.6488	2.5127	2.7704	2.0099
MOSEK 10.2.0	2.4241	2.3193	4.3832	18.7699	16.3591	12.2785	11.9517	17.8730

3.8. Sensitivity Study

To evaluate the robustness of the proposed MILP model, a sensitivity analysis was performed by modifying the elements of set C, which directly affects the β sizing parameter. Since traditional sensitivity analysis applies strictly to linear models, an approximate parametric analysis was employed to evaluate how variations in the selection of standard curves influenced the optimization results, evaluating their impact on the objective function, the number of parameters and variables, and the computational times. This approach provided insights into the impact of the different curve configurations on the relay coordination. To facilitate graphical representation and comparative analysis, the standard protection curves

were grouped and labeled using Curve Identifiers (Cid), as detailed in Table 21. This setup systematically reduced the number of curves available in Set C.

Table 21. Mapping of standard protection curves to Cid identifiers.

Cid	Curves on the Set C
C1	STI, SI, VI, EI, LTI, IEEE-LTI, IEEE-LTVI, IEEE-LTEI, IEEE-MI, IEEE-VI, IEEE-EI, IEEE-STI, IEEE-STEI
C2	STI, SI, VI, EI, LTI, IEEE-LTI, IEEE-LTVI, IEEE-LTEI, IEEE-MI, IEEE-VI, IEEE-EI, IEEE-STI
C3	STI, SI, VI, EI, LTI, IEEE-LTI, IEEE-LTVI, IEEE-LTEI, IEEE-MI, IEEE-VI, IEEE-EI
C4	STI, SI, VI, EI, LTI, IEEE-LTI, IEEE-LTVI, IEEE-LTEI, IEEE-MI, IEEE-VI
C5	STI, SI, VI, EI, LTI, IEEE-LTI, IEEE-LTVI, IEEE-LTEI, IEEE-MI
C6	STI, SI, VI, EI, LTI, IEEE-LTI, IEEE-LTVI, IEEE-LTEI
C7	STI, SI, VI, EI, LTI, IEEE-LTI, IEEE-LTVI
C8	STI, SI, VI, EI, LTI, IEEE-LTI
C9	STI, SI, VI, EI, LTI
C10	STI, SI, VI, EI
C11	STI, SI, VI
C12	STI, SI

Figure 3 illustrates the sensitivity analysis of the model concerning the number of available standard curves (Cid). Cid represents the set of curves available for the model, where Cid 1 included all 13 curves, while Cid 12 was restricted to only two curves (STI and SI). The model was systematically adjusted to assess its sensitivity to the number of available curves in set *C*. The results indicate that the number of curves directly impacted the objective function, particularly when the set was significantly reduced. However, in the initial stages, the objective function remained largely unaffected, suggesting that the model retained sufficient flexibility when a moderate number of curves were available.

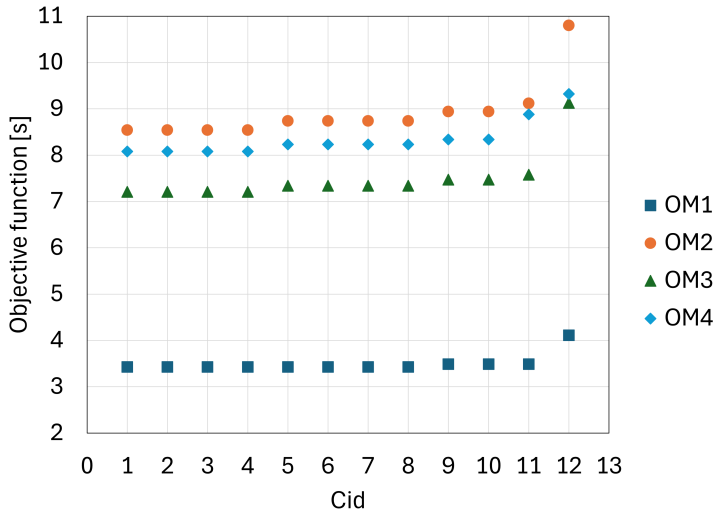


Figure 3. Variation in the objective function across different operating modes (OMs) as a function of the number of active protection curves (Cid).

Table 22 illustrates how the size of the parameter arrays β_{fic} and variable TMS_{ic} changed as a function of the active curves (*Cid*). It is evident that the size of these parameters decreased exponentially as the number of available curves was reduced. This reduction directly impacted the objective function (OF) across all operating modes (OM), leading

to tripping time deterioration as fewer curves remained available. Specifically, for OM1, the objective function remained relatively stable until Cid 9, where a slight increase was observed, while in OM2, OM3, and OM4, the degradation started earlier, becoming more pronounced for Cid 12, where two curves were enabled, STI and SI.

Furthermore, the computation time (measured in seconds) increased with the parameter and variables size, but not in a strictly linear fashion. While larger parameter arrays required more computation, the execution time varied due to solver optimizations and internal heuristics. Comparing Table 22 with Figure 3, it can be seen that the reduction in available curves led to an increasing trend in objective function values, particularly for OM2, OM3, and OM4, reinforcing the notion that a larger set of curves provides better optimization flexibility and improved protection coordination performance.

Table 22. Impact of the number of available protection curves (Cid) on various parameters, objective function (OF), and computational time across different operating modes (OMs).

Cid	Sizing		OM1		OM2		OM3		OM4	
	β_{fic}	TMS_{ic}	OF	Time	OF	Time	OF	Time	OF	Time
C1	975	195	3.43	0.138	8.54	0.3736	7.21	0.2638	8.08	0.1173
C2	900	180	3.43	0.1259	8.54	0.1873	7.21	0.1722	8.08	0.4559
C3	825	165	3.43	0.0688	8.54	0.2099	7.21	0.167	8.08	0.1027
C4	750	150	3.43	0.1112	8.54	0.1701	7.21	0.1031	8.08	0.211
C5	675	135	3.43	0.0739	8.74	0.1882	7.34	0.1832	8.23	0.1793
C6	600	120	3.43	0.0816	8.74	0.1259	7.34	0.1524	8.23	0.0925
C7	525	105	3.43	0.0907	8.74	0.1112	7.34	0.0866	8.23	0.0637
C8	450	90	3.43	0.0344	8.74	0.0275	7.34	0.0263	8.23	0.0276
C9	375	75	3.49	0.0391	8.94	0.0267	7.47	0.0229	8.34	0.0249
C10	300	60	3.49	0.0276	8.94	0.0223	7.47	0.0258	8.34	0.0218
C11	225	45	3.49	0.0235	9.12	0.0216	7.58	0.0186	8.88	0.0213
C12	150	30	4.11	0.0242	10.8	0.0186	9.13	0.0182	9.32	0.018

Figure 4 displays the results of the sensitivity analysis conducted on the Coordination Time Interval (CTI) parameter. The objective function (OF), measured in seconds, was evaluated for different CTI values ranging from 0.20 to 0.50 seconds across four operating modes (OM1–OM4). In all cases, an increasing trend was observed in the OF as the CTI grew. This behavior was expected, as larger CTI values generally enhance selectivity by increasing the time margin between the operation of primary and backup protective devices. However, this improvement in selectivity typically comes at the cost of longer total operation times, which is reflected in the increase in the objective function. Figure 4 highlights the distinct behavior of each OM under varying CTI conditions, offering insights into their relative performance in balancing selectivity and operational speed.

Table 23 complements the sensitivity analysis depicted in Figure 4 by presenting the numerical results for the objective function (OF) and the corresponding computation times (in seconds) for each optimization model (OM1–OM4) across a range of Coordination Time Interval (CTI) values. The data confirm the increasing trend of the objective function as CTI increased, consistent with the graphical trends previously discussed. Additionally, the table reveals differences in computational performance among the models. For instance, OM1 consistently exhibited the lowest OF values and the shortest computation times, suggesting a higher efficiency in terms of both coordination time and solution speed. In contrast, models such as OM2 and OM4 generally achieved higher OF values, with more variability in their solution times. These results provide quantitative insights into how each model balanced selectivity, as influenced by CTI, with computational efficiency.

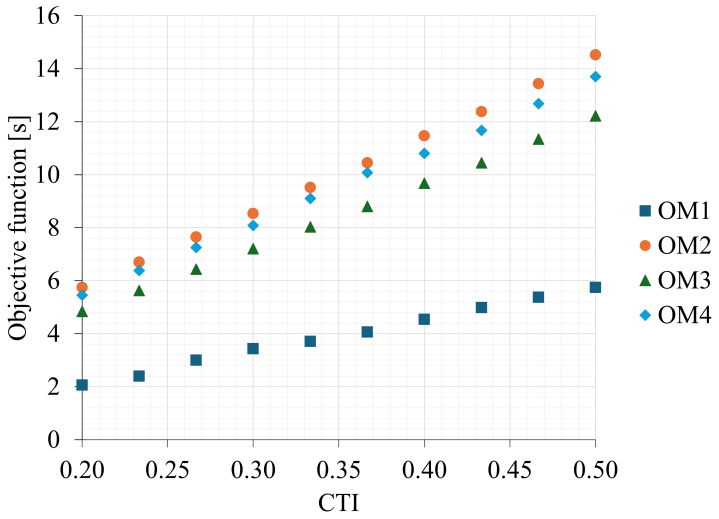


Figure 4. Objective function values obtained for varying CTI levels across different OMs.

Table 23. Computation time and objective function values for different Coordination Time Interval (CTI) levels across all OMs.

CTI	OM1		OM2		OM3		OM4	
	OF	Time	OF	Time	OF	Time	OF	Time
0.2000	2.06	0.074	5.75	0.172	4.84	0.445	5.45	0.549
0.2333	2.40	0.102	6.70	0.531	5.63	0.315	6.38	0.422
0.2667	3.00	0.080	7.65	0.222	6.44	0.384	7.25	0.266
0.3000	3.43	0.116	8.54	0.306	7.21	0.541	8.08	0.191
0.3333	3.71	0.069	9.52	0.122	8.03	0.235	9.10	0.226
0.3667	4.06	0.055	10.45	0.175	8.80	0.193	10.08	0.460
0.4000	4.54	0.053	11.47	0.301	9.68	0.170	10.80	0.253
0.4333	4.98	0.052	12.38	0.155	10.45	0.119	11.67	0.056
0.4667	5.37	0.047	13.43	0.093	11.34	0.093	12.68	0.080
0.5000	5.75	0.056	14.52	0.075	12.22	0.083	13.70	0.163

Figure 5 illustrates the relationship between the CTI and the average computation time obtained from the different OMs. Table 23 presents the computation times required for each CTI value. For this analysis, the average time across all OMs was calculated for each CTI value and subsequently plotted, revealing a linear relationship between average computation time and CTI. A negative linear trend was observed, indicating that higher average computation times are generally associated with lower CTI values. The fitted regression line is given by $y = -0.9812x + 0.5487$, with a coefficient of determination $R^2 = 0.8424$, suggesting a strong inverse correlation. This result implies that more time is required to solve the optimization problem when lower CTI values are imposed. In this case, the increased computational effort for small CTI values is due to the fact that tighter coordination requirements impose stricter constraints on the system and the optimization model. Conversely, higher CTI values can be interpreted as a relaxation of the problem. In optimization, relaxation refers to the process of simplifying a problem by loosening certain constraints, thereby making it more tractable. A common example is relaxing binary or integer variables to continuous domains, allowing the use of linear or convex programming techniques. Although a solution to the relaxed problem may not always be feasible for the original formulation, it can offer useful bounds and insights into the solution space. In this study, the optimal solution was feasible for all instances due to the MILP structure of the model and the solver's capabilities. While optimality was guaranteed, smaller CTI values led to longer solution times because the selectivity constraint became more restrictive in

the inequality formulation. Note that unlike the parametric sensitivity analysis of the beta parameter, where the number of variables and parameters in the model varied, in this analysis, the variables and parameters remain the same size. Therefore, the solution time is primarily a function of the solver's ability to find the optimal solution to the model.

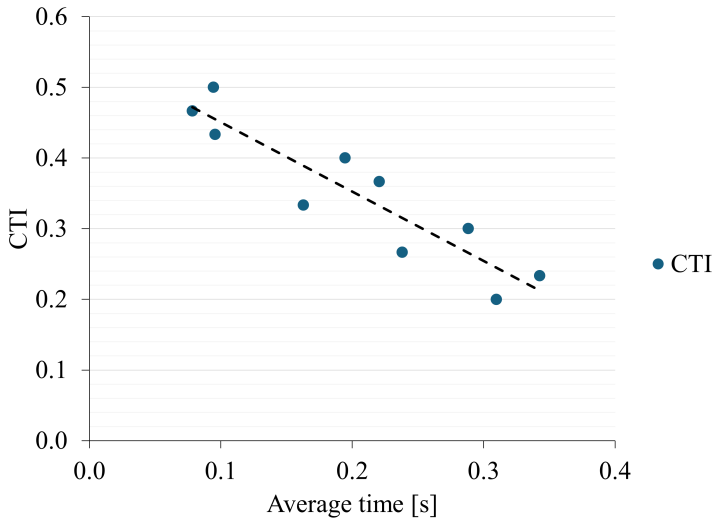


Figure 5. Linear regression between average computation time and CTI.

4. Conclusions

This study presents a MILP model for the optimal coordination of DOCRs in MGs, addressing the challenges posed by the integration of DERs. The proposed model minimizes the total tripping time of DOCRs, while ensuring selectivity, leveraging both IEC and IEEE standard characteristic curves. The results demonstrate that integrating both standards significantly reduced the fault-clearing times compared to using only IEEE curves, highlighting the importance of curve diversity in enhancing protection coordination.

The model was tested on the IEC benchmark microgrid, and its performance was evaluated across multiple operational modes, including grid-connected and islanded scenarios. The findings show that the proposed approach achieved faster fault isolation and improved coordination, contributing to the reliability and resilience of microgrid protection systems. Additionally, the study highlights the computational efficiency of the various solvers available through the NEOS Server, providing insights into solver performance for large-scale MILP problems.

A sensitivity analysis was conducted to evaluate the impact of the number of available protection curves on the optimization results. The findings indicate that a larger set of protection curves provides greater flexibility in achieving optimal coordination, particularly in more complex operational scenarios. However, as the number of available curves decreased, the objective function deteriorated, and the computational burden varied nonlinearly. Moreover, since the model explicitly considers different operating modes (OMs), it inherently captures the effect of varying fault levels, which change between islanded and grid-connected conditions. This reinforces the robustness of the proposed approach in adapting to different fault scenarios.

The sensitivity analysis of the CTI highlighted a clear trade-off between coordination strictness and computational effort. The observed inverse linear relationship between CTI and average computation time indicates that enforcing lower CTI values, which reflect more stringent selectivity requirements, leads to increased solver effort, due to tighter constraints in the optimization model. Conversely, higher CTI values act as a relaxation mechanism, simplifying the solution process. Despite this trade-off, unlike β sensitivity analyses involving changes in model size, this experiment maintained a fixed model structure,

confirming that the observed variation in computation time was primarily driven by the solver's ability to handle increased constraint tightness, balancing selectivity requirements with computational efficiency in practical protection coordination scenarios.

Future work could explore the integration of hybrid protection schemes and real-time communication strategies to further enhance the robustness of microgrid protection systems. The findings of this study underscore the potential of advanced optimization techniques in addressing the evolving challenges of modern power systems, paving the way for more resilient and efficient microgrids.

Author Contributions: Conceptualization, L.F.S.-M. and S.D.S.-Z.; methodology, L.F.S.-M. and S.D.S.-Z.; software, L.F.S.-M. and S.D.S.-Z.; validation, S.D.S.-Z., J.M.L.-L. and N.M.-G.; formal analysis, L.F.S.-M.; investigation, L.F.S.-M., J.M.L.-L. and S.D.S.-Z.; resources, L.F.S.-M.; data curation, L.F.S.-M. and S.D.S.-Z.; writing—original draft preparation, L.F.S.-M.; writing—review and editing, J.M.L.-L. and N.M.-G.; visualization, L.F.S.-M. and J.M.L.-L.; supervision, N.M.-G.; project administration, N.M.-G.; funding acquisition, L.F.S.-M. and N.M.-G. All authors have read and agreed to the published version of the manuscript.

Funding: This research was funded by the Sistema General de Regalías of Colombia within the framework project "Formación a nivel de posgrado de capital humano para el desarrollo socioeconómico del departamento de Antioquia" (Project No. BPIN 2021000100098).

Data Availability Statement: The original contributions presented in this study are included in the article. Further inquiries can be directed to the corresponding authors.

Acknowledgments: The authors express their sincere appreciation to the Universidad de Antioquia and the Institución Universitaria Pascual Bravo for their institutional support and commitment, which were instrumental in the successful development of this work.

Conflicts of Interest: The authors declare no conflicts of interest.

Abbreviations

The following abbreviations are used in this manuscript:

ANSI	American National Standards Institute
CB	Circuit Breaker
CBC	COIN-OR Branch and Cut
CPLEX	IBM ILOG CPLEX Optimization Studio
CTI	Coordination Time Interval
CTR	Current Transformer Ratio
DER	Distributed Energy Resources
DFIG	Doubly-Fed Induction Generator
DG	Distributed Generator
DL	Distribution Line
DOCR	Directional Overcurrent Relay
GA	Genetic Algorithm
HIL	Hardware-in-the-Loop
IEC	International Electrotechnical Commission
IEEE	Institute of Electrical and Electronics Engineers
MG	Microgrid
MILP	Mixed-Integer Linear Programming
MINLP	Mixed-Integer Nonlinear Programming
NEOS	Network-Enabled Optimization System
OM	Operating Mode
PCC	Point of Common Coupling
PSM	Plug Setting Multiplier
PV	Photovoltaic

SCC	Standard Characteristic Curve
TMS	Time Multiplier Setting
TR	Transformer

References

1. Liu, R.; Ding, L.; Xue, C.; Li, Y. Small-signal modelling and analysis of microgrids with synchronous and virtual synchronous generators. *IET Energy Syst. Integr.* **2024**, *6*, 45–61. [CrossRef]
2. Shen, X.; Shen, C.; Huang, W.; Xu, Y. Dynamic mater-slave control strategy for transient coordination of inverter based microgrids under asymmetric faults. *Int. J. Electr. Power Energy Syst.* **2024**, *161*, 110191. [CrossRef]
3. Zhao, H.; Shuai, Z.; Ge, J.; Luo, A.; Wu, W.; Shen, Z.J. Asymmetrical Fault Current Calculation Method and Influencing Factors Analysis of Droop-Controlled Inverters. *CSEE J. Power Energy Syst.* **2024**, *10*, 562–573. [CrossRef]
4. Yao, W.; Pei, C.; Chi, R.; Shao, W.; Li, B. Presynchronization control for ship microgrid of merchant marine inverters based on VSG algorithm with MFAC. *Trans. Inst. Meas. Control* **2024**, *46*, 1858–1870. [CrossRef]
5. Abdi, G.; Jirdehi, M.A.; Mehrjerdi, H. Optimal coordination of overcurrent relays in microgrids using meta-heuristic algorithms NSGA-II and harmony search. *Sustain. Comput. Inform. Syst.* **2024**, *43*, 101020. [CrossRef]
6. Kandil, T. Investigation of the Impact of Fault Characteristics on the Cost-Effectiveness of Doubly Fed Induction Generator-Based Wind Systems in Withstanding Low-Voltage Ride-Through. *Sustainability* **2024**, *16*, 5812. [CrossRef]
7. Kumar, K.; Kar, S. An efficient protection scheme for microgrid using ROC of differential admittance angle. *Electr. Power Syst. Res.* **2024**, *227*, 109969. [CrossRef]
8. Pola, S.; Azzouz, M.A.; Mirhassani, M. Synchronverters with Fault Ride-Through Capabilities for Reliable Microgrid Protection during Balanced and Unbalanced Faults. *IEEE Trans. Sustain. Energy* **2024**, *15*, 1663–1676. [CrossRef]
9. Wang, L.; Zhang, K.; Bi, W.; Wang, Y.; Li, Y.; Mao, W. Indirect Coordinated Attack Against Relay via Load-Side Power Electronics and Its Defense Strategy. *IEEE Trans. Ind. Inform.* **2024**, *20*, 5112–5124. [CrossRef]
10. Gómez-Luna, E.; De La Cruz, J.; Vasquez, J.C. New Approach for Validation of a Directional Overcurrent Protection Scheme in a Ring Distribution Network with Integration of Distributed Energy Resources Using Digital Twins. *Energies* **2024**, *17*, 1677. [CrossRef]
11. Niranjan, P.; Choudhary, N.K.; Singh, N.; Singh, R.K. Optimal Coordination of Dual-Setting Directional Over Current Relay in Microgrid Considering Multi-Parametric Characteristics. *J. Oper. Autom. Power Eng.* **2025**, *13*, 174–183. [CrossRef]
12. Sadeghi, S.; Hashemi-Dezaki, H. Optimal communication-free protection of meshed microgrids using non-standard overcurrent relay characteristics considering different operation modes and configurations based on N-1 contingency. *Sustain. Cities Soc.* **2024**, *106*, 105376. [CrossRef]
13. Mohamed Abdullah, J.; Sumathi, V. Implementation and proficiency analysis of enhanced graph algorithm for DC microgrid applications. *Sci. Rep.* **2024**, *14*, 14476. [CrossRef]
14. Wu, Y.; Wang, W.; Tang, F.; Wu, X. Adaptive virtual admittance control of bidirectional DC/DC converters for DC bus voltage ripple suppression in DC microgrids. *Int. J. Electr. Power Energy Syst.* **2024**, *159*, 110045. [CrossRef]
15. Jahanbani, H.; Razavi, F.; Nafisi, H. Presenting an innovative single-setting adaptive protection method for AC microgrid with wind turbine. *Electr. Eng.* **2024**. [CrossRef]
16. Alasali, F.; El-Naily, N.; Mustafa, H.Y.; Loukil, H.; Saad, S.M.; Salah Saidi, A.; Holderbaum, W. Digital twin for advanced optimal coordination scheme of distance and Dual-Stage overcurrent relays. *Ain Shams Eng. J.* **2025**, *16*, 103197. [CrossRef]
17. Sati, T.E.; Azzouz, M.A.; Shaaban, M.F. Adaptive harmonic-based protection coordination for inverter-dominated isolated microgrids considering N-1 contingency. *Int. J. Electr. Power Energy Syst.* **2024**, *156*, 109750. [CrossRef]
18. Peter, N.; Gupta, P.; Goel, N. Intelligent strategies for microgrid protection: A comprehensive review. *Appl. Energy* **2025**, *379*, 124901. [CrossRef]
19. Reiz, C.; Leite, J.B.; Gouveia, C.S.; Javadi, M.S. Protection system planning in distribution networks with microgrids using a bi-level multi-objective and multi-criteria optimization technique. *Electr. Power Syst. Res.* **2024**, *228*, 109966. [CrossRef]
20. Heidary, A.; Popov, M.; Moghim, A.; Ghaffarian Niasar, M.; Lekic, A. The Principles of Controlled DC-Reactor Fault Current Limiter for Battery Energy Storage Protection. *IEEE Trans. Ind. Electron.* **2024**, *71*, 1525–1534. [CrossRef]
21. Asghari, M.; Ameli, A.; Ghafouri, M.; Kirakosyan, A. An optimal cyber–physical attack strategy on DC microgrids. *Int. J. Electr. Power Energy Syst.* **2024**, *157*, 109900. [CrossRef]
22. Ghanem, Z.; Alasali, F.; Ei-Naily, N.; Loukil, H.; Mustafa, H.Y.; Saad, S.M.; Saidi, A.S.; Holderbaum, W. Advanced Microgrid Protection Utilizing Zero Sequence Components with Hard-ware-in-the-Loop Testing. *IEEE Access* **2025**, *13*, 7623–7636. [CrossRef]
23. Vazquez, J.; Rodriguez Segura, E.J.J.; Arau Roffiel, J.E.; Vazquez, N. Bidirectional protection for DC systems based on di/dt behavior. *IEEE Lat. Am. Trans.* **2024**, *22*, 945–951. [CrossRef]
24. Yan, L.; Zhao, Z.; Ullah, Z.; Deng, X.; Zhang, Y.; Ali Shah, W. Optimization of optical storage VSG control strategy considering active power deviation and virtual inertia damping parameters. *Ain Shams Eng. J.* **2024**, *15*, 103131. [CrossRef]

25. Wang, K.; Xue, Y.; Shahidehpour, M.; Chang, X.; Li, Z.; Zhou, Y.; Sun, H. Resilience-Oriented Two-Stage Restoration Considering Coordinated Maintenance and Reconfiguration in Integrated Power Distribution and Heating Systems. *IEEE Trans. Sustain. Energy* **2025**, *16*, 124–137. [CrossRef]
26. Giri, N.; Nayak, P.; Kumar Mallick, R.; Mishra, S.; Flah, A.; Kraiem, H.; Prokop, L.; Kanan, M. Wavelet-Based ensembled intelligent technique for a better quality of fault detection and classification in AC microgrids. *Energy Convers. Manag. X* **2024**, *24*, 100813. [CrossRef]
27. Singh, B.P.; Goyal, S.K.; Siddiqui, S.A.; Shrivastava, D.R.; Singh, S.; A. Alotaibi, M.; Malik, H.; García Márquez, F.P.; Afthanorhan, A. A Novel Approach for Enhanced Real-Time Event Diagnosis for Grid Connected Microgrid with Multiple Distributed Energy Resources (DERs). *Int. J. Math. Eng. Manag. Sci.* **2024**, *9*, 557–580. [CrossRef]
28. Tiwari, S.P. An efficient protection scheme for critical fault detection in microgrid under uncertain scenarios using deep learning algorithm. *Electr. Eng.* **2024**. [CrossRef]
29. Tajdinian, M.; Behdani, B.; Tanbhir Hoq, M.; Popov, M. Sub-Cycle Phase Angle-Oriented Algorithm for Identifying Fault Direction in Renewable-Rich MV Distribution Grids. *IEEE Trans. Instrum. Meas.* **2024**, *73*, 9005211. [CrossRef]
30. Alasali, F.; El-Naily, N.; Loukil, H.; El Deen Omran, E.; Holderbaum, W.; Elhaffar, A.; Saidi, A.S. The Performance and Robustness of Power Protection Schemes for Grid-Connected PV Systems Under Varied Smart Inverter Controllers. *Int. J. Energy Res.* **2024**, *2024*, 6805410. [CrossRef]
31. Dewangan, F.; Biswal, M. An enhanced algorithm for detection of HIAF in active distribution networks and real-time analysis. *Electr. Power Syst. Res.* **2025**, *238*, 111108. [CrossRef]
32. Bui, D.M.; Le, P.D.; Nguyen, H.M. Development of a Novel Backup Fault Protection Algorithm for Low-Voltage DC Microgrids based on Local Measurements and Chi-square Statistics. *Eng. Technol. Appl. Sci. Res.* **2024**, *14*, 15106–15120. [CrossRef]
33. Khan, J.A.; Mahmood, T. Robust Unified Multi Diverse Protection Schemes for Low Voltage Microgrid. *J. Electr. Eng. Technol.* **2024**, *19*, 1079–1096. [CrossRef]
34. Tripathy, M.; Kishore, C.; Sharma, S.; Wang, L. A novel differential protection scheme for AC microgrid based on loss function. *Electr. Power Syst. Res.* **2025**, *238*, 110973. [CrossRef]
35. Biswal, S.; Samantaray, S.R. Relay Coordination Scheme in Microgrids Based on Non-Standard Tripping Curve of DOCRs with Multiple Setting Groups. *IEEE Trans. Ind. Inform.* **2024**, *20*, 5737–5749. [CrossRef]
36. Cisneros-Saldana, J.I.D.; Samal, S.; Begovic, M.M.; Samantaray, S.R. On Protection Schemes for AC Microgrids: Challenges and Opportunities. *IEEE Trans. Ind. Appl.* **2024**, *60*, 4843–4854. [CrossRef]
37. Singh, P.; Kumar, U.; Kumar Choudhary, N.; Singh, N. Advancements in Protection Coordination of Microgrids: A Comprehensive Review of Protection Challenges and Mitigation Schemes for Grid Stability. *Prot. Control. Mod. Power Syst.* **2024**, *9*, 156–183. [CrossRef]
38. Desai, J.P. Microgrid Harmonic-Restrained Dual Slope Differential Protection. *J. Inst. Eng. (India) Ser. B* **2024**, *105*, 297–308. [CrossRef]
39. Serna-Montoya, L.F.; Saldarriaga-Zuluaga, S.D.; López-Lezama, J.M.; Muñoz-Galeano, N. Optimal Coordination of Directional Overcurrent Relays in Microgrids Considering European and North American Curves. *Energies* **2024**, *17*, 5887. [CrossRef]
40. Kumar, N.; Jain, D.K. Optimal coordination of overcurrent relays for microgrid operation using JAYA algorithm. *e-Prime-Adv. Electr. Eng. Electron. Energy* **2024**, *7*, 100467. [CrossRef]
41. Merabet, O.; Kheldoun, A.; Bouchahdane, M.; Eltom, A.; Kheldoun, A. An adaptive protection coordination for microgrids utilizing an improved optimization technique for user-defined DOCRs characteristics with different groups of settings considering N-1 contingency. *Expert Syst. Appl.* **2024**, *248*, 123449. [CrossRef]
42. Urdaneta, A.; Restrepo, H.; Marquez, S.; Sanchez, J. Coordination of directional overcurrent relay timing using linear programming. *IEEE Trans. Power Deliv.* **1996**, *11*, 122–129. [CrossRef]
43. Hong, Y.Y.; Yu, C.W.; Lee, Y.D.; Jiang, J.L.; Wang, S.S. Coordination of protective relays in distribution systems considering uncertainty caused by renewables and demands based on orthogonal experiments. *Sustain. Energy Grids Netw.* **2023**, *36*, 101206. [CrossRef]
44. Karimkhan Zand, H.; Mazlumi, K.; Bagheri, A.; Abdali, A. Optimal coordination of DOCRs in microgrid via contingency reduction mechanism and clustering algorithms considering various network topologies based on N-2 contingencies. *Expert Syst. Appl.* **2023**, *234*, 121061. [CrossRef]
45. Martin, K.T.; Marchesan, A.C.; De Araújo, O.C.B.; Cardoso, G.; Da Silva, M.F. Mixed Integer Linear Programming Applied to Adaptive Directional Overcurrent Protection Considering N-1 Contingency. *IEEE Trans. Ind. Appl.* **2023**, *59*, 2807–2821. [CrossRef]
46. *IEEE Std C37.112-1996 (R2001)*; IEEE Standard Inverse-Time Characteristic Equations for Overcurrent Relays (ANSI 51). Institute of Electrical and Electronics Engineers: New York, NY, USA, 1996. [CrossRef]
47. *IEC/IEEE 60255-118-1:2018*; IEEE/IEC International Standard—Measuring Relays and Protection Equipment—Part 118-1: Synchrophasor for Power Systems—Measurements. IEEE: Piscataway, NJ, USA, 2018; pp. 1–78. [CrossRef]

48. *IEEE Std C37.112-2018 (Revision of IEEE Std C37.112-1996)* ; IEEE Standard for Inverse-Time Characteristics Equations for Overcurrent Relays. IEEE: Piscataway, NJ, USA, 2019. [CrossRef]
49. Ustun, T.S.; Ozansoy, C.; Zayegh, A. Modeling of a Centralized Microgrid Protection System and Distributed Energy Resources According to IEC 61850-7-420. *IEEE Trans. Power Syst.* **2012**, *27*, 1560–1567. [CrossRef]
50. Kar, S.; Samantaray, S.R.; Zadeh, M.D. Data-Mining Model Based Intelligent Differential Microgrid Protection Scheme. *IEEE Syst. J.* **2017**, *11*, 1161–1169. [CrossRef]
51. *IEC 60909*; Short-Circuit Currents in Three-Phase A.C. Systems. International Electrotechnical Commission: Geneva, Switzerland, 2001.
52. Santos-Ramos, J.E.; Saldarriaga-Zuluaga, S.D.; López-Lezama, J.M.; Muñoz-Galeano, N.; Villa-Acevedo, W.M. Microgrid Protection Coordination Considering Clustering and Metaheuristic Optimization. *Energies* **2024**, *17*, 210. [CrossRef]
53. *IEC 61850*; Communication Networks and Systems for Power Utility Automation. International Electrotechnical Commission: Geneva, Switzerland, 2003.
54. Czyzyk, J.; Mesnier, M.; More, J. The NEOS Server. *IEEE Comput. Sci. Eng.* **1998**, *5*, 68–75. Available online: https://neos-server.org/neos/index.html (accessed on 27 January 2025). [CrossRef]

Disclaimer/Publisher's Note: The statements, opinions and data contained in all publications are solely those of the individual author(s) and contributor(s) and not of MDPI and/or the editor(s). MDPI and/or the editor(s) disclaim responsibility for any injury to people or property resulting from any ideas, methods, instructions or products referred to in the content.